Photovoltaic restoration of sight with high visual acuity

Henri Lorach[1–3,8], Georges Goetz[1,4,8], Richard Smith[5], Xin Lei[4], Yossi Mandel[6], Theodore Kamins[4], Keith Mathieson[7], Philip Huie[1,2], James Harris[4], Alexander Sher[5,9] & Daniel Palanker[1,2,9]

Patients with retinal degeneration lose sight due to the gradual demise of photoreceptors. Electrical stimulation of surviving retinal neurons provides an alternative route for the delivery of visual information. We demonstrate that subretinal implants with 70-μm-wide photovoltaic pixels provide highly localized stimulation of retinal neurons in rats. The electrical receptive fields recorded in retinal ganglion cells were similar in size to the natural visual receptive fields. Similarly to normal vision, the retinal response to prosthetic stimulation exhibited flicker fusion at high frequencies, adaptation to static images and nonlinear spatial summation. In rats with retinal degeneration, these photovoltaic arrays elicited retinal responses with a spatial resolution of 64 ± 11 μm, corresponding to half of the normal visual acuity in healthy rats. The ease of implantation of these wireless and modular arrays, combined with their high resolution, opens the door to the functional restoration of sight in patients blinded by retinal degeneration.

Retinal degenerative diseases such as age-related macular degeneration and retinitis pigmentosa lead to blindness due to the gradual loss of photoreceptors, while the inner retinal neurons survive to a large extent[1,2], albeit with some rewiring[3,4]. Retinal prostheses aim at restoring sight by electrical stimulation of these surviving neurons. In the epiretinal approach, the primary targets of stimulation are the retinal ganglion cells (RGCs)[5,6], whereas subretinal stimulation elicits visual responses via inner retinal neurons (primarily bipolar cells)[7–9]. Both approaches have recently been approved for clinical use, but these systems involve bulky implanted electronics with trans-scleral cables and require very complex surgeries. In addition, visual acuity with the epiretinal system (ARGUS II, Second Sight Inc., Sylmar, California, USA) is no better than 20/1,260 (ref. 6), and the visual percepts elicited in patients are distorted because of axonal stimulation[10]. Subretinal prostheses (Alpha IMS, Retina Implant AG, Reutlingen, Germany) provide similar acuity levels, mostly below 20/1,000, except for one patient who reached 20/550 (ref. 11).

We have developed an alternative approach to retinal prosthetics in which photovoltaic subretinal pixels convert pulsed light into electric current, thereby enabling a completely wireless implant[12,13]. Bright pulsed illumination is provided by image projection from video goggles, and photophobic effects are avoided through the use of near-infrared (NIR, 880–915 nm) light. Pulsed illumination is necessary to provide charge-balanced stimulation, which is critical for the electrochemical biocompatibility of the prosthesis. Optical delivery of the visual information preserves the natural link between ocular movement and image perception, unlike with systems in which the electrodes are connected to an external camera via serial telemetry. Since these implants are wireless, multiple small (1–2 mm in width) arrays can be placed under the retina via a small retinotomy to tile a large visual field, thereby greatly simplifying surgery, compared to all other implants wired to extraocular power supplies. Photovoltaic arrays with two or three diodes per pixel can safely elicit and modulate retinal responses, both *in vitro* and *in vivo*, in both normally sighted (wild-type Long-Evans, WT) and blind (Royal College of Surgeons, RCS) rats[12,14,15]. In this animal model of retinal degeneration, a progressive loss of photoreceptors is triggered by the inability of the retinal pigment epithelium to phagocytose shed photoreceptor outer segments[16].

In the present study, we evaluate the spatiotemporal characteristics of prosthetic vision, including two of its most important properties: the spatial resolution of the retinal response *in vitro* and the corresponding visual acuity achieved *in vivo*.

RESULTS

Electrical receptive fields

The prosthetic devices used throughout the study consist of a hexagonal array of 70-μm-wide pixels separated by 5-μm trenches, corresponding to a 65-μm pitch between adjacent rows (**Fig. 1a,b**). Pixels consist of several photodiodes connected in series, delivering anodic-first, charge-balanced pulses of current. Individual return electrodes were incorporated into each pixel to localize the stimulation current. A resistance between the active and return electrodes acts like a shunt resistor and helps discharge the electrodes between the pulses (**Fig. 1c**).
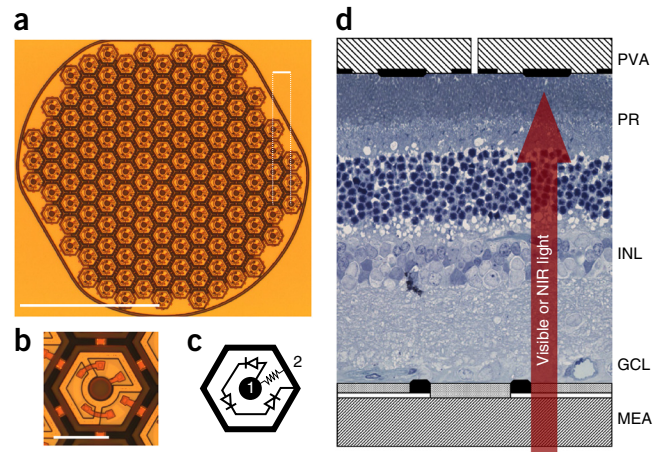
We conducted an *in vitro* evaluation of the spatial resolution of the retinal response to photovoltaic stimulation and to visible light by recording from hundreds of retinal ganglion cells (RGCs) in the rat retina using a large-scale multielectrode array system[17] (**Fig. 1d**, **Supplementary Fig. 1**). In a normal retina, visual information transduced by the photoreceptors is further processed in the inner nuclear layer before it is transmitted to the ganglion cells. The visual receptive

[1]Hansen Experimental Physics Laboratory, Stanford University, Stanford, California, USA. [2]Department of Ophthalmology, Stanford University, Stanford, California, USA. [3]Inserm UMR_S968, Institut de la Vision, Paris, France. [4]Department of Electrical Engineering, Stanford University, Stanford, California, USA. [5]Santa Cruz Institute for Particle Physics, University of California Santa Cruz, Santa Cruz, California, USA. [6]The Mina & Everard Goodman Faculty of Life Sciences, Bar Ilan University, Israel. [7]Institute of Photonics, University of Strathclyde, Glasgow, UK. [8]These authors contributed equally to this work. [9]These authors jointly supervised this work. Correspondence should be addressed to G.G. (ggoetz@stanford.edu).

Figure 1 Photovoltaic array and *in vitro* experimental setup. (**a**) Photograph of a single module of the photovoltaic prosthesis. It is composed of 70-μm-wide pixels separated by 5-μm trenches arranged in a 1-mm-wide hexagonal pattern, with the adjacent rows separated by 65 μm. Scale bars: top right-hand corner, 65 μm; bottom left-hand corner, 500 μm. (**b**) Close-up photograph of a 70-μm-wide pixel. Scale bar, 50 μm. (**c**) The wiring diagram for each pixel. Each pixel consists of two to three (shown here) photodiodes connected in series between the central active (1) and surrounding return (2) electrode. (**d**) Schematic representation of a healthy rat retina sandwiched between a transparent multielectrode array (MEA) which records from the ganglion cell layer (GCL) and the photovoltaic array (PVA). Visible light stimulates the photoreceptors (PR), while much brighter pulsed NIR (880–915 nm) illumination generates biphasic pulses of current in the photovoltaic pixels, stimulating cells in the inner nuclear layer (INL).

fields (vRFs) of different ganglion cell types form complementary mosaics over the retinal surface[18–21] and define the characteristics of retinal processing. Here, we compared vRFs (**Fig. 2a**), measured in the healthy rat retina using a visible light spatiotemporal binary white noise stimulus projected onto the photoreceptor layer[22], to the response properties to electrical stimulation of both healthy WT and degenerated RCS retina. For prosthetic stimulation of the retina, we mapped the electrical receptive fields (eRFs) of the RGCs (**Fig. 2b,d**) using a sparse NIR binary noise stimulus projected onto the photovoltaic pixels (**Supplementary Fig. 2** and Online Methods). Gray levels in **Figure 2b,c** encode the average number of network-mediated action potentials elicited in the RGC. Transient electrical currents produced by the photovoltaic implant appear as large stimulation artifacts on the multielectrode array recordings and prevent detection of possible short-latency action potentials resulting from the direct stimulation of ganglion cells (**Supplementary Fig. 2**). However, the stimulation parameters used in this study have previously been shown to selectively elicit network-mediated responses[14,23,24]. The response latencies we observed with photovoltaic activation (**Supplementary Fig. 2**) were consistent with stimulation originating at the photoreceptor terminals or in the inner nuclear layer. A previous study demonstrated that blocking all synaptic connections eliminates RGC responses, whereas blocking transmission between photoreceptors and ON-bipolar cells does not affect the response from ON RGCs[12]. This result, together with the observation that efficient *in vivo* stimulation of the retina occurs in animals fully devoid of photoreceptors[14,15], supports the notion that the retinal stimulation induced by our subretinal photovoltaic array occurs at the level of bipolar cells.

The average eRF diameter was 248 ± 59 μm in WT and 203 ± 63 μm in RCS retinas (**Fig. 2d**). With a visible light stimulus, the average vRF diameter in WT retinas was 244 ± 32 μm (**Fig. 2d**), not substantially

different from the eRF diameter. Despite recording from a variety of RGC types in WT retina (ON and OFF, transient and sustained, brisk and sluggish cells[25]) with a variety of receptive field sizes, we did not observe any correlation between eRF and vRF sizes, making it difficult to predict what eRF diameter to expect in RGCs with very small receptive fields, such as midget cells in human retina.

Although the majority of eRFs consisted only of an excitatory central component, some eRFs measured in both WT and RCS retinas (10 out of 92 neurons in WT retinas and 6 out of 48 neurons in RCS retinas) had a more complex structure, displaying both a localized and a diffuse, 'donut-shaped' component. Both the localized and the diffuse components of the response were excitatory in nature, but with different latencies (**Fig. 2c**, **Supplementary Fig. 3**). The eRFs with a diffuse component were not included in the calculation of the eRF average size (**Fig. 2d**, triangles).

Retinal response to grating contrast reversal

Although measurement of the spatial extent of electrical receptive fields obtained with a sparse white noise provides an indication of achievable spatial resolution, it does not take into account possible nonlinear effects of presenting more complex stimuli. To account for such effects, we characterized retinal responses to square gratings of various spatial frequencies for which we periodically reversed light and dark stripes, using visible light and photovoltaic stimulation (see Online Methods). This type of stimulus is routinely used for measuring visual acuity *in vivo*[26–28]. Experiments were conducted with RCS retinas for photovoltaic stimulation (4-ms pulses, 5-mW/mm²-irradiance NIR pulses) and with WT retinas for
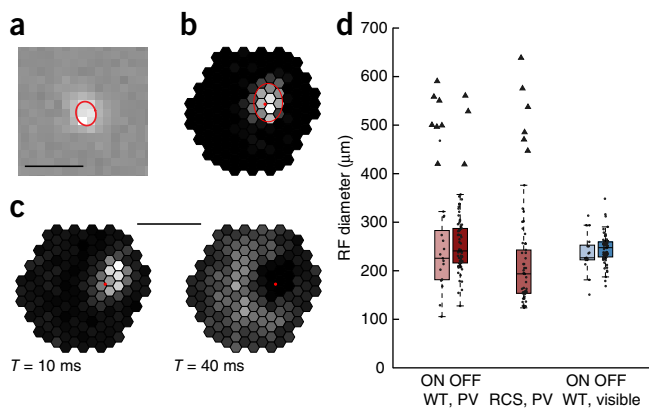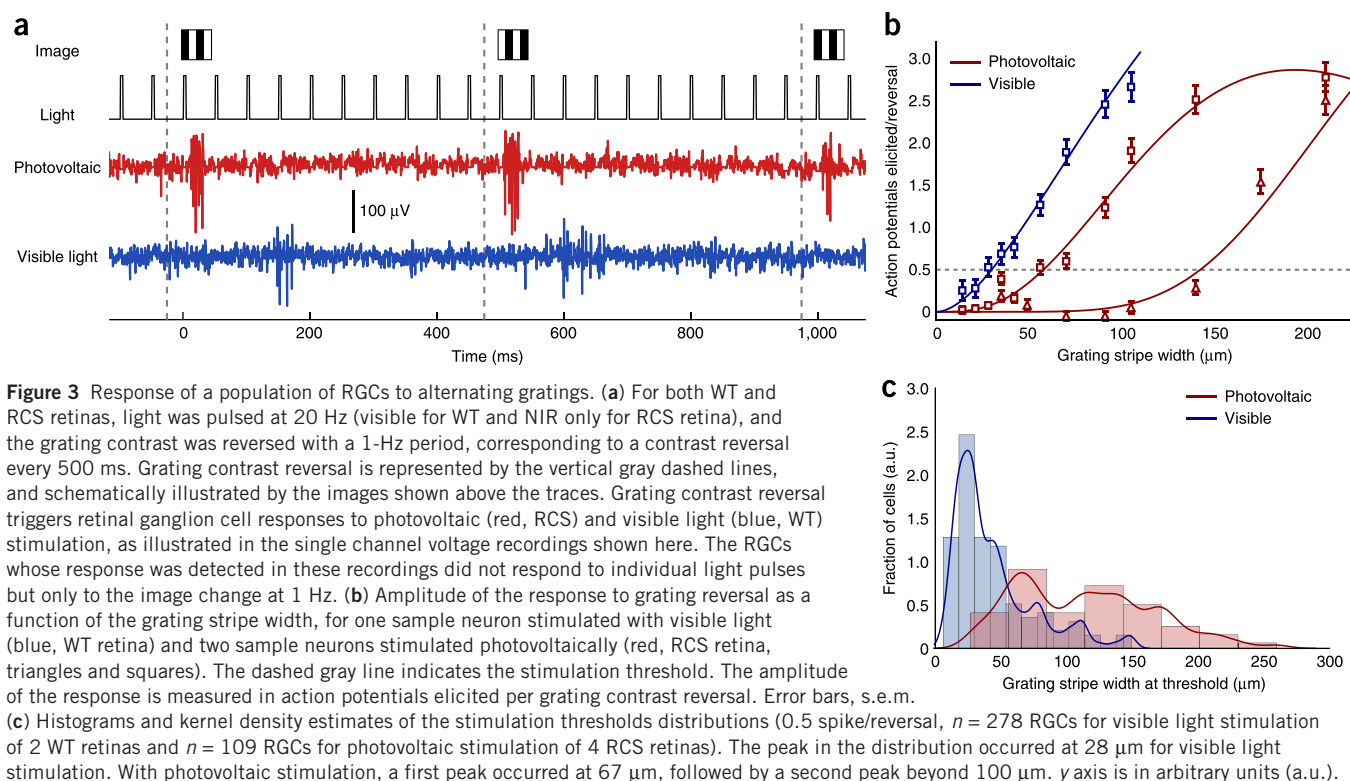

Figure 2 Natural and prosthetic receptive fields of RGCs. (**a**) The visible light receptive field (vRF) of an ON RGC in a WT retina. The red ellipsoid corresponds to the 1 s.d. contour of a Gaussian fit. Scale bar, 500 μm. (**b**) The electric receptive field (eRF) of an RGC in a WT retina. Gray levels encode the number of spikes in response to stimulation of different pixels: black = 0, white = maximum (2.4 action potentials/light pulse). The estimated position of the cell body (soma) is indicated by the red dot. (**c**) An eRF with an early local response (time *T* = 10 ms post-stimulus) followed by a later diffuse response (time *T* = 40 ms post-stimulus) in a WT retina. Scale bar, 500 μm. (**d**) Distribution of eRF diameters (red, photovoltaic, *n* = 92 RGCs for 3 WT retinas and *n* = 48 RGCs for 4 RCS retinas) and vRF diameters (blue, visible, *n* = 92 RGCs for 3 WT retinas) in healthy (WT) and RCS retinas depicted in Tukey box plots. For eRFs measured with photovoltaic (PV) stimulation, circles correspond to localized eRFs, triangles to eRFs with a diffuse component. In the WT retina, RGCs were separated between ON-center and OFF-center types.
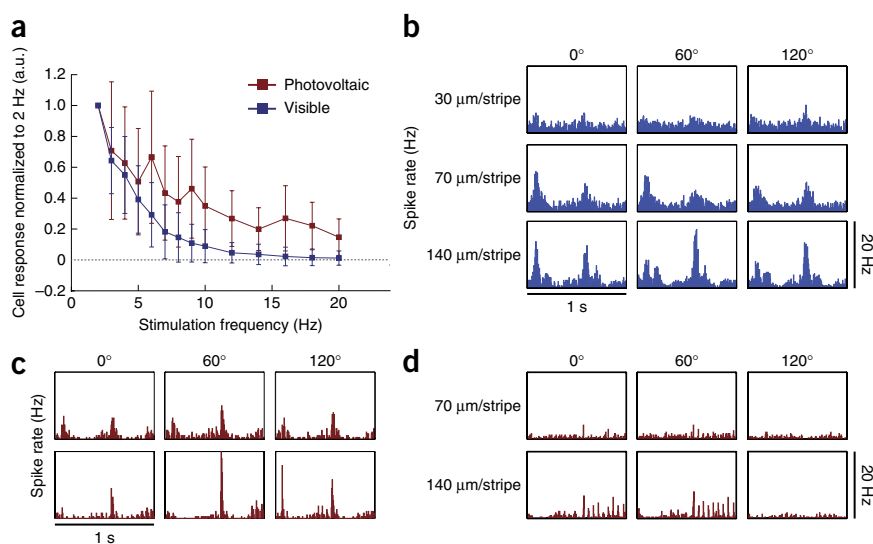
Figure 3 Response of a population of RGCs to alternating gratings. (**a**) For both WT and RCS retinas, light was pulsed at 20 Hz (visible for WT and NIR only for RCS retina), and the grating contrast was reversed with a 1-Hz period, corresponding to a contrast reversal every 500 ms. Grating contrast reversal is represented by the vertical gray dashed lines, and schematically illustrated by the images shown above the traces. Grating contrast reversal triggers retinal ganglion cell responses to photovoltaic (red, RCS) and visible light (blue, WT) stimulation, as illustrated in the single channel voltage recordings shown here. The RGCs whose response was detected in these recordings did not respond to individual light pulses but only to the image change at 1 Hz. (**b**) Amplitude of the response to grating reversal as a function of the grating stripe width, for one sample neuron stimulated with visible light (blue, WT retina) and two sample neurons stimulated photovoltaically (red, RCS retina, triangles and squares). The dashed gray line indicates the stimulation threshold. The amplitude of the response is measured in action potentials elicited per grating contrast reversal. Error bars, s.e.m. (**c**) Histograms and kernel density estimates of the stimulation thresholds distributions (0.5 spike/reversal, $n = 278$ RGCs for visible light stimulation of 2 WT retinas and $n = 109$ RGCs for photovoltaic stimulation of 4 RCS retinas). The peak in the distribution occurred at 28 μm for visible light stimulation. With photovoltaic stimulation, a first peak occurred at 67 μm, followed by a second peak beyond 100 μm. *y* axis is in arbitrary units (a.u.).

visible light stimulation (10-ms, 591-nm pulses, low photopic regime); the width of the square-wave grating stripes was varied from 7 to 300 μm. Visible and NIR images were projected with 20-Hz flicker frequency and 1-Hz grating alternation period, corresponding to an image change every 500 ms (**Fig. 3a**). Photovoltaic arrays require pulsed illumination to provide charge-balanced pulses of electric current, and we also applied visible light in the same way for a better comparison between the two types of stimulation.

Electrical stimulation of RCS retina resulted in a continuum of responses, ranging from a combination of strong transient responses to the alternating gratings with very weak responses to individual pulses at 20 Hz (**Fig. 3a**), to more robust responses to every stimulation pulse. In the WT retina we observed very little, if any response to

individual pulses of visible light at 20 Hz, and strong responses to the grating contrast reversal. Thus, a substantial fraction (about half) of the RGCs in RCS retinas under electrical stimulation, and virtually all RGCs in WT retinas under visual stimulation, responded to the grating contrast reversal and not to every pulse of light (**Fig. 3a**). Just as the healthy retina stops responding to high-frequency pulsed visible stimuli through a phenomenon known as flicker fusion that leads to adaptation to static images, the degenerate retina stimulated via a sub-retinal prosthesis exhibits a similar adaptation to static images. Flicker fusion nonetheless appeared less complete with the prosthetic system, as a number of neurons maintained a weak response to NIR pulses at 20 Hz (**Fig. 4a**). In the WT retina, the steady-state response was negligible at the same frequency (**Fig. 4a**). It remains to be explored whether more complete flicker fusion can be achieved with prosthetic stimulation at higher repetition rates.

To assess the spatial resolution of the retinal response to photovoltaic and visible light stimulation, we quantified the strength of the

Figure 4 Single-unit RGC responses to alternating gratings. (**a**) Average steady-state response of RGCs to pulsed stimulation of varying frequency in arbitrary units (a.u.) ($n = 178$ RGCs for visible light stimulation of two WT retinas and $n = 45$ RGCs for photovoltaic stimulation of two RCS retinas). Error bars, s.d. (**b**) The response (spike rate) of a single RGC to 1-Hz contrast reversal of square gratings of varying phase projected with visible light onto WT retina. (**c,d**) Two-sample single-unit responses to photovoltaic stimulation of RCS retina. With photovoltaic stimulation (20-Hz, 4-ms pulses), responses varied between RGCs that exhibited strong flicker fusion (**c**) and RGCs that did not (**d**).

RGC response to grating contrast reversal as a function of the stripe width (see Online Methods). This response, measured in action potentials elicited per grating contrast reversal, decreased with increasing spatial frequency of the gratings, for both visible light and electrical stimulation (**Fig. 3b**).

Next, we defined the stimulation threshold as the grating stripe size that results in a 50% probability of eliciting an action potential, time-locked to the grating contrast reversal (see Online Methods). The distribution of thresholds measured with visible light stimulation peaked at a stripe width of 28 μm in one of the retinas studied and at a stripe width of 48 μm in the other (**Supplementary Fig. 4**). This difference is most likely due to variation in eccentricity of the retinal sections we recorded from. With photovoltaic stimulation, the distribution exhibited a peak at 67 μm per stripe, with a large tail extending to widths greater than 100 μm (**Fig. 3c**, 109 RGCs, $n = 4$ retinas; see also **Supplementary Table 1**).

Responses of the neurons to gratings narrower than their receptive field diameter, whether electrical or visible, can be explained by nonlinear interactions in receptive field subunits[25,29,30]. For visible light, the peak corresponds to neurons responding to each phase of the grating alternation. In typical RGCs, a frequency-doubled response became detectable at 30 μm/stripe and was clearly evident at 70 μm/stripe (**Fig. 4b**). At 140 μm/stripe, frequency doubling was still present, but one of the phases of the grating usually exhibited a strong asymmetry of the peaks, with one peak, termed the linear (or f1) component of the response, stronger than the other (f2). This classical frequency doubling of the response is indicative of nonlinear spatial summation[25,30].

Similarly, with NIR stimulation, neurons responded to gratings with 70-μm stripes with frequency doubling. For neurons that exhibited strong flicker fusion (**Fig. 4c**), a transient frequency-doubled response could be seen for all phases of the grating at 70 μm/stripe. At 140 μm/stripe, the frequency doubling typically still took place for one phase, whereas a strong linear response could also be seen for other phases of the grating. Therefore, nonlinear summation occurs inside the RGC electrical receptive fields, and the size of the nonlinear subunits is comparable to the pixel pitch (**Fig. 1a**). RGCs that did not exhibit flicker fusion usually had a dominant linear response for 140 μm/stripe gratings (**Fig. 4d**), with action potentials time-locked to every pulse delivered to the retina. For these RGCs, the response at 70 μm/stripe was negligible.

Among RCS neurons that responded to gratings narrower than 75 μm/stripe, 71% exhibited frequency doubling in their responses, consistent with nonlinear summation in the receptive field subunits. In these RGCs, the amplitudes of the response to each half period of the grating reversal did not differ by more than 25%, for at least one of the phases. All neurons that exhibited complete flicker fusion with photovoltaic stimulation (that is, no response to 20-Hz pulses when a static image was displayed, similar to the response to visible light in the normal retina) also exhibited high resolution: they responded to grating contrast reversal with stripe widths smaller than 100 μm.

Subretinal implants *in vivo*

For *in vivo* testing of prosthetic vision, we implanted the photovoltaic arrays subretinally in 16 rats ($n = 9$ WT, $n = 7$ RCS, **Supplementary Table 1**). Fluorescein angiography confirmed normal retinal blood perfusion above the implant (**Fig. 5a**). Optical coherence tomography (OCT) performed 1 week after surgery demonstrated close and stable proximity of the inner nuclear layer to the implant (**Fig. 5b**).

In WT rats, the presence of the subretinal implant caused degeneration of the photoreceptors above the chip, whereas the inner nuclear layer (INL) and ganglion cell layer (GCL) were well preserved[14]. This local outer retinal degeneration is likely due to separation of the photoreceptor outer segments from the retinal pigment epithelium and isolation of the photoreceptor outer segments from choroidal perfusion.

Cortical response thresholds and dynamic range

We assessed the response of the visual system by recording visually evoked potentials (VEPs) induced either by the implant activated with pulsed NIR light (eVEP) or by visible light projected onto normal retina (**Fig. 5c** and Online Methods). We used a camera mounted on a slit lamp to visualize the stimulus on the retina and control the position of the beam relative to the implant.
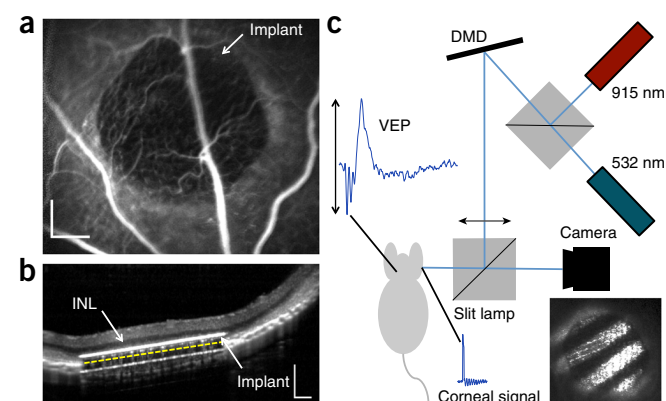
Photovoltaic stimulation thresholds (see Online Methods[14]) did not differ substantially between WT and RCS rats. With 10-ms pulses and a 2-Hz repetition rate, the stimulation thresholds were 0.55 ± 0.08 mW/mm^2 for both WT and RCS animals. The eVEP amplitude increased with irradiance between 0.125 mW/mm^2 and 1 mW/mm^2, saturating at higher light intensity (**Fig. 6a**). Increasing the pulse duration from 1 ms to 10 ms also increased the cortical response, which saturated at longer pulse durations (**Fig. 6b**). Therefore, the cortical response to photovoltaic subretinal stimulation can be modulated either by irradiance or by pulse duration over an order-of-magnitude–wide dynamic range.

Visual acuity

One of the established methods for assessing visual acuity in animals and in human infants is based on the cortical response to alternating gratings of various spatial frequencies, recorded through

Figure 5 *In vivo* subretinal implantation and stimulation setup. (**a**) Fluorescein angiography of a RCS retina 1 week after surgery demonstrates normal retinal blood perfusion above the implant with no leakage. The implant is opaque to visible light and masks the choroidal fluorescence in the implanted area. Scale bar, 200 μm. (**b**) In an implanted RCS retina, OCT shows good preservation of the inner retina, with the inner nuclear layer (INL) located ~20 μm above the upper surface of the implant (white line). The implant (30 μm in thickness) appears thicker than it actually is because of its high refractive index. The yellow dashed line illustrates the actual position of the back side of the implant, which is located on top of the retinal pigment epithelium. Horizontal and vertical scale bars, 200 μm each. (**c**) Stimulation system for VEP recordings. The visible (532 nm) and NIR (915 nm) lasers illuminate the digital micromirror device (DMD), which generates the images projected onto the retina, as shown in the photograph (inset). The cortical activity (VEP signal) is recorded via transcranial electrodes. The simultaneously recorded corneal potential shows the stimulation pulses from the implant.
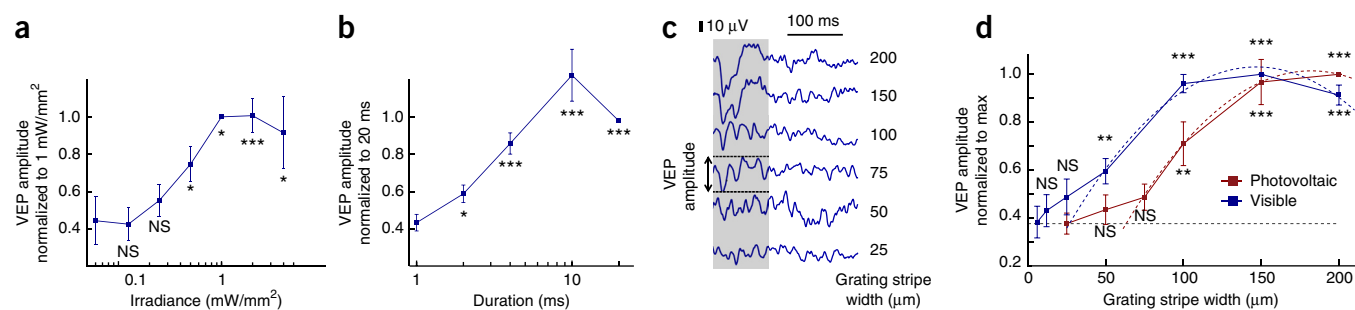
Figure 6 *In vivo* prosthetic stimulation and visual acuity. (**a,b**) VEP modulation by irradiance (**a**) and pulse duration (**b**) under full-field illumination (*n* = 9 WT animals and *n* = 3 RCS animals in both irradiance and pulse duration measurements). (**c**) Sample VEP traces recorded from an RCS animal corresponding to different grating stripe widths. We defined the VEP amplitude as the peak-to-peak variation of the signal during the first 100 ms after grating alternation (gray shaded area) for prosthetic stimulation. (**d**) VEP amplitude for visible gratings (blue) and photovoltaic (prosthetic) stimulation (red) was measured as a function of grating stripe widths. The acuity limit and its associated uncertainty, estimated as the crossing point of the parabolic fits with the noise level (dashed lines), corresponded to 27 ± 9 μm/stripe for visible light and 64 ± 11 μm/stripe for prosthetic stimulation (*n* = 7 WT animals with visible light and *n* = 7 RCS animals with prosthetic stimulation). Error bars, s.e.m. NS, not significant; *P < 0.05; ** *P* < 0.01; ***P < 0.001, one-tailed Welch *t*-test performed against the lowest irradiance, duration and grating size groups in **a**, **b** and **d**, respectively.

visually evoked potentials (VEPs)[26,27]. This method matches well the visual acuity measured in behavioral tests[28,31].

We recorded the cortical responses to such alternating NIR patterns in implanted RCS rats (**Fig. 6c**) and to the same patterns presented with visible light in WT animals on healthy retina outside the implanted area (data not shown). The square-wave grating patterns were projected using 4-ms pulses at a 40-Hz repetition rate and the contrast was reversed at 1 Hz. Grating stripe width was varied from 6 μm to 200 μm. We defined the VEP amplitude as the peak-to-peak variation of the signal during the first 100 ms following grating alternation (gray shaded area in **Fig. 6c**) for prosthetic stimulation. Visible light triggered slower and longer-lasting responses, and we measured the amplitude during the first 300 ms after alternation. The VEP amplitude decreased with increasing spatial frequency (that is, decreasing stripe width) for both visible and electrical stimulation (**Fig. 6d**).

With electrical stimulation, 100-μm stripes elicited robust responses in all (*n* = 7) RCS rats, and eVEP amplitudes were significantly different from the noise level (*P* < 0.01, one-tailed Welch *t*-test). With a grating of 75 μm, the signal amplitude was still above the noise level (by 29%), but the difference was not statistically significant (*P* = 0.097). In WT animals, responses to visible light stripes of 50 μm were significantly above the noise level (*P* < 0.05), but gratings with 25-μm stripes did not elicit significant responses (*P* = 0.17) (**Fig. 6d**).

We estimated the acuity limit by extrapolating the measured data down to the noise level (**Fig. 6d** and Online Methods). For prosthetic vision in RCS rats, the limit and corresponding uncertainty (see Online Methods) was 64 ± 11 μm per stripe, as compared to 27 ± 9 μm per stripe in WT animals stimulated with visible light. The data obtained in RCS and WT rats correspond to 0.47 and 1.1 cycles per degree (cpd), respectively, in close agreement with the 1- to 1.2-cpd visual acuity of pigmented rats reported in the literature[26–28,31].

To confirm that these responses conveyed spatial information rather than charge accumulation or an illumination imbalance between the two phases of the grating, we recorded the stimulus pulses on the cornea to assess the amount of charge delivered by the implant during each phase of the grating. We then applied uniform full-field stimulation with variable light intensity, producing stimuli of similar amplitudes but devoid of spatial content (**Supplementary Fig. 5**). This control experiment was conducted in RCS rats. For all grating sizes, the equivalent spatially uniform stimulus did not trigger any detectable VEP response (see definition in Online Methods), confirming that the

grating response was due to spatial modulation. Additionally, RCS rats did not respond to alternating gratings projected onto the implanted area with visible light, and also did not respond to pulsed infrared light projected away from the implant (**Supplementary Fig. 6**).

DISCUSSION

In this work, we used photovoltaic implants in which the pixels were redesigned based on a recent optimization of the subretinal stimulation protocols[24], so as to deliver anodic-first pulses of current[12,14]. The resulting cortical activation threshold in WT and RCS rats implanted with 70-μm pixel arrays was 0.55 mW/mm² with 10-ms pulses—four times lower than the threshold previously reported by our group using implants that delivered cathodic-first pulses[12,14] and more than two orders of magnitude below the ocular safety limit for the 880- to 915-nm wavelength range[32,33] (Online Methods). Low stimulation thresholds are important for the development of compact, safe and efficient video goggles that would be used to activate retinal implants in human subjects[34]. Low stimulation thresholds also indicate that pixel size could be reduced further by about a factor of 2, thereby enabling higher spatial resolution. However, stimulation thresholds are likely to depend on the characteristics of the retinal network and extent of degeneration. At the highest settings used in this study, stimulation for many hours at a time *in vitro* and *in vivo* did not decrease responsiveness or produce any signs of tissue damage, confirming the safety of the NIR irradiation settings. Although the results with rats are certainly encouraging, further testing in larger animals will be required to assess safety and efficacy of stimulation before human use.

Similarity of the stimulation thresholds between WT and RCS rats *in vivo* is likely due to local degeneration of the photoreceptors above the implants[14]. In WT animals, a progressive loss of photoreceptors caused by the implant is likely triggered by the chronic separation of photoreceptors from the retinal pigment epithelium. A few weeks after implantation, in both WT and RCS rats, the outer retina degenerated and bipolar cells achieved similar proximity to the electrodes.

In natural vision, the retina acts as a temporal bandpass filter transmitting local changes in luminance within a certain range of temporal frequencies. The low end of this frequency band represents the effect of fading of static images, which typically occurs within seconds, for example when eye movements are disabled[35]. The high end of this band corresponds to flicker fusion (image fusion) at high frequencies, resulting in a continuous perception of movies with a frame rate

exceeding 20 Hz. A similar effect of fading of a static image produced by high-frequency network-mediated electrical stimulation of the retina has previously been referred to as 'desensitization'[8], and it was considered detrimental for vision restoration. However, we argue that our *in vitro* and *in vivo* results demonstrate that desensitization can be interpreted as flicker fusion and adaptation to static images, a natural feature of vision. With high flicker frequency in our experiments (20–40 Hz), the retina responded primarily to luminance transitions of the image rather than to individual pulses of light. Therefore, the network-mediated retinal response to electrical stimulation appears to preserve three features of normal vision: (1) fusion of high-frequency flicker, (2) adaptation to static images, and (3) response to image changes at lower frequencies, similar to the natural 'event-based' language of the retina[36].

One of the most important characteristics of vision in general, and in prosthetic restoration of sight in particular, is visual acuity. Both the epiretinal and subretinal implants that have been tested in clinical trials enabled rather low acuity, which varied greatly among patients[6,11]. The majority of patients could not read and, among the few who could, visual acuity was mostly below 20/1,200, except for a single patient who was reported to achieve 20/550 (ref. 11). Local return electrodes in our photovoltaic pixels provide much tighter confinement of the electric field compared to the monopolar electrodes in other implants. This helps reduce cross-talk between neighboring electrodes, thereby increasing contrast and spatial resolution of the stimulation[37,38].

Photovoltaic pixels elicited highly localized responses in both normal and degenerated (RCS) retinas, and the electrical receptive fields of individual RGCs in the RCS retina had a size similar to those of the visually evoked receptive fields in the WT retina. A minority of RGCs (10 out of 92 in WT and 6 out of 48 in RCS retinas) responded with an additional diffuse component involving mechanisms that remain to be explored. However, since RGCs responded to alternating gratings down to 28 µm/stripe with visible light, and to 67 µm/stripe with photovoltaic stimulation, it appears that the resolution-limiting factor is the pixel size. Reducing the pixel size further might therefore improve localization of the retinal response.

Measurements of the cortical and retinal responses to alternating gratings demonstrated that, much as with normal vision, a degenerated retina stimulated via the prosthetic device could extract features smaller than the RGC receptive fields. This nonlinear summation of subunits within the ganglion cell receptive fields[39–43] is another important function of the retinal neural network that is preserved with subretinal stimulation. More generally, the retinal response to prosthetic stimulation with stripe widths similar to the pixel spacing demonstrates excellent localization of this relatively complex stimulus to the 70-µm pixels, without much interference from neighboring electrodes.

Extrapolating from the measured sizes of electrical receptive fields and their nonlinear subunits to expected perceptual acuity in human subjects is difficult. It is yet unclear whether high acuity vision in rats is mediated by midget-like retinal ganglion cells with small receptive fields—as appears to be the case in primates[44]—or whether population effects are responsible. To provide single-pixel resolution for central vision in humans, midget cells in the fovea (within 2.5 degrees of eccentricity) would have to respond to stimulation from a single pixel only. Because of our limited ability to record from cells with very small receptive fields in the rat retina, we could not show directly that small ganglion cells can be stimulated in such a spatially selective fashion. Our results are likely to be applicable to more peripheral regions of the primate retina where ensemble responses of ganglion cells might play a role in improving spatial resolution beyond their individual receptive

field sizes. Within a few months of retinal degeneration in rats, the size of the RGC electrical receptive fields did not increase compared to those in the healthy retina. However, it remains to be seen whether retinal rewiring at more advanced stages of degeneration in human subjects will affect the spatial confinement of the stimulation and its thresholds.

The spatial frequency cutoff measured *in vivo* was similar to that measured *in vitro*, but the *in vivo* data were easier to interpret in terms of perceptual visual acuity restored[26,27]. Extrapolation of the measured data down to the noise level yielded an estimate of the acuity limit of 64 ± 11 µm/stripe or 0.47 cpd for prosthetic stimulation, matching the pixel row pitch of the implant (65 µm). This is only two times lower than the normal acuity limit in rats: 27 ± 9 µm/stripe or 1.1 cpd. The human eye is approximately 5 times larger than the rat eye, and a resolution of 64 µm per stripe on a human retina corresponds to 2.4 cpd, which is geometrically equivalent to 20/250 visual acuity as measured with alternating gratings. As the stimulation thresholds were much lower than the safety limits, it would be possible to decrease pixel size further, thereby supporting even higher spatial resolution.

As opposed to acuity measurements in clinical trials, which revealed large variability among patients[11], our results were highly consistent between animals: all the rats responding to full field stimulation also responded to gratings with a 100-µm stripe width. Further behavioral experiments with animals will nonetheless be needed to verify whether electrophysiological measurements of prosthetic visual acuity correspond to behavioral and perceptual endpoints as well as they do with conventional visual stimulation[26,28,31]. Ultimately, visual acuity and other aspects of prosthetic visual function in human subjects will need to be established by careful psychophysical examination.

METHODS

Methods and any associated references are available in the online version of the paper.

Note: Any Supplementary Information and Source Data files are available in the online version of the paper.

AUTHOR CONTRIBUTIONS

X.L. fabricated the subretinal implants under the supervision of T.K., K.M., J.H. and D.P. G.G., R.S., D.P. and A.S. designed the *in vitro* experiments. R.S. and G.G. performed the *in vitro* experiments. H.L., D.P. and Y.M. designed the *in vivo* experiments. H.L., Y.M. and P.H. performed the *in vivo* experiments. G.G. and H.L. analyzed the data. G.G., H.L., A.S. and D.P. wrote the paper.

1. Santos, A. *et al.* Preservation of the inner retina in retinitis pigmentosa: a morphometric analysis. *Arch. Ophthalmol.* **115**, 511–515 (1997).

2. Humayun, M.S. *et al.* Morphometric analysis of the extramacular retina from postmortem eyes with retinitis pigmentosa. *Invest. Ophthalmol. Vis. Sci.* **40**, 143–148 (1999).

3. Marc, R.E., Jones, B.W., Watt, C.B. & Strettoi, E. Neural remodeling in retinal degeneration. *Prog. Retin. Eye Res.* **22**, 607–655 (2003).

4. Jones, B.W. & Marc, R.E. Retinal remodeling during retinal degeneration. *Exp. Eye Res.* **81**, 123–137 (2005).

5. Behrend, M.R., Ahuja, A.K., Humayun, M.S., Chow, R.H. & Weiland, J.D. Resolution of the epiretinal prosthesis is not limited by electrode size. *IEEE Trans. Neural Syst. Rehabil. Eng.* **19**, 436–442 (2011).

6. Humayun, M.S. *et al.* Interim results from the international trial of Second Sight's visual prosthesis. *Ophthalmology* **119**, 779–788 (2012).

7. Zrenner, E. Fighting blindness with microelectronics. *Sci. Transl. Med.* **5**, 210–216 (2013).

8. Jensen, R.J. & Rizzo, J.F. Thresholds for activation of rabbit retinal ganglion cells with a subretinal electrode. *Exp. Eye Res.* **83**, 367–373 (2006).

9. Zrenner, E. *et al.* Subretinal electronic chips allow blind patients to read letters and combine them to words. *Proc. Biol. Sci.* **278**, 1489–1497 (2011).

10. Nanduri, D. *et al.* Frequency and amplitude modulation have different effects on the percepts elicited by retinal stimulation. *Invest. Ophthalmol. Vis. Sci.* **53**, 205–214 (2012).

11. Stingl, K. *et al.* Artificial vision with wirelessly powered subretinal electronic implant alpha-IMS. *Proc. Biol. Sci.* **280**, 20130077 (2013).

12. Mathieson, K. *et al.* Photovoltaic retinal prosthesis with high pixel Density. *Nat. Photonics* **6**, 391–397 (2012).

13. Wang, L. *et al.* Photovoltaic retinal prosthesis: implant fabrication and performance. *J. Neural Eng.* **9**, 046014 (2012).

14. Mandel, Y. *et al.* Cortical responses elicited by photovoltaic subretinal prostheses exhibit similarities to visually evoked potentials. *Nat. Commun.* **4**, 1980 (2013).

15. Lorach, H. *et al.* Performance of photovoltaic arrays in-vivo and characteristics of prosthetic vision in animals with retinal degeneration. *Vision Res.* doi:10.1016/j.visres.2014.09.007 (2014).

16. Vollrath, D. *et al.* Correction of the retinal dystrophy phenotype of the RCS rat by viral gene transfer of Mertk. *Proc. Natl. Acad. Sci. USA* **98**, 12584–12589 (2001).

17. Litke, A.M. *et al.* What does the eye tell the brain? Development of a system for the large-scale recording of retinal output activity. *IEEE Trans. Nucl. Sci.* **51**, 1434–1440 (2004).

18. Devries, S.H. & Baylor, D.A. Mosaic arrangement of ganglion cell receptive fields in rabbit retina. *J. Neurophysiol.* **78**, 2048–2060 (1997).

19. Pillow, J.W. *et al.* Spatio-temporal correlations and visual signalling in a complete neuronal population. *Nature* **454**, 995–999 (2008).

20. Dacey, D.M. Origins of perception: retinal ganglion cell diversity and the creation of parallel visual pathways. in *The Cognitive Neurosciences* (ed. Gazzaniga, M.S.) 281–301 (MIT Press, 2004).

21. Wässle, H. Parallel processing in the mammalian retina. *Nat. Rev. Neurosci.* **5**, 747–757 (2004).

22. Chichilnisky, E.J. A simple white noise analysis of neuronal light responses. *Network* **12**, 199–213 (2001).

23. Fransen, J.W., Pangeni, G., Pardue, M.T. & McCall, M.A. Local signaling from a retinal prosthetic in a rodent retinitis pigmentosa model in vivo. *J. Neural Eng.* **11**, 046012 (2014).

24. Boinagrov, D., Pangratz-Fuehrer, S., Goetz, G. & Palanker, D. Selectivity of direct and network-mediated stimulation of the retinal ganglion cells with epi-, sub- and intra-retinal electrodes. *J. Neural Eng.* **11**, 026008 (2014).

25. Heine, W.F. & Passaglia, C.L. Spatial receptive field properties of rat retinal ganglion cells. *Vis. Neurosci.* **28**, 403–417 (2011).

26. Silveira, L.C.L., Heywood, C.A. & Cowey, A. Contrast sensitivity and visual acuity of the pigmented rat determined electrophysiologically. *Vision Res.* **27**, 1719–1731 (1987).

27. Harnois, C., Bodis-Wollner, I. & Onofrj, M. The effect of contrast and spatial frequency on the visual evoked potential of the hooded rat. *Exp. Brain Res.* **57**, 1–8 (1984).

28. Prusky, G.T., West, P.W.R. & Douglas, R.M. Behavioral assessment of visual acuity in mice and rats. *Vision Res.* **40**, 2201–2209 (2000).

29. Enroth-Cugell, C. & Robson, J.G. The contrast sensitivity of retinal ganglion cells of the cat. *J. Physiol. (Lond.)* **187**, 517–552 (1966).

30. Petrusca, D. *et al.* Identification and characterization of a Y-like primate retinal ganglion cell type. *J. Neurosci.* **27**, 11019–11027 (2007).

31. Dean, P. Visual pathways and acuity in hooded rats. *Behav. Brain Res.* **3**, 239–271 (1981).

32. Loudin, J.D., Cogan, S.F., Mathieson, K., Sher, A. & Palanker, D.V. Photodiode circuits for retinal prostheses. *IEEE Trans. Biomed. Circuits Syst.* **5**, 468–480 (2011).

33. Delori, F.C., Webb, R.H. & Sliney, D.H. Maximum permissible exposures for ocular safety (ANSI 2000), with emphasis on ophthalmic devices. *J. Opt. Soc. Am. Sci. Vis.* **24**, 1250–1265 (2007).

34. Goetz, G.A., Mandel, Y., Manivanh, R., Palanker, D.V. & Cizmar, T. Holographic display system for restoration of sight to the blind. *J. Neural Eng.* **10**, 056021 (2013).

35. Martinez-Conde, S., Macknik, S.L. & Hubel, D.H. The role of fixational eye movements in visual perception. *Nat. Rev. Neurosci.* **5**, 229–240 (2004).

36. Lorach, H. *et al.* Artificial retina: the multichannel processing of the mammalian retina achieved with a neuromorphic asynchronous light acquisition device. *J. Neural Eng.* **9**, 066004 (2012).

37. Joucla, S. & Yvert, B. Improved focalization of electrical microstimulation using microelectrode arrays: a modeling study. *PLoS ONE* **4**, e4828 (2009).

38. Loudin, J.D. *et al.* Optoelectronic retinal prosthesis: system design and performance. *J. Neural Eng.* **4**, S72–S84 (2007).

39. Victor, J.D., Shapley, R.M. & Knight, B.W. Nonlinear analysis of cat retinal ganglion cells in the frequency domain. *Proc. Natl. Acad. Sci. USA* **74**, 3068–3072 (1977).

40. Victor, J.D. & Shapley, R.M. The nonlinear pathway of Y ganglion cells in the cat retina. *J. Gen. Physiol.* **74**, 671–689 (1979).

41. Anishchenko, A. *et al.* Receptive field mosaics of retinal ganglion cells are established without visual experience. *J. Neurophysiol.* **103**, 1856–1864 (2010).

42. Gollisch, T. & Meister, M. Eye smarter than scientists believed: neural computations in circuits of the retina. *Neuron* **65**, 150–164 (2010).

43. Demb, J.B., Zaghloul, K. & Haarsma & Sterling, P. Bipolar cells contribute to nonlinear spatial summation in the brisk-transient (Y) ganglion cells in mammalian retina. *J. Neurosci.* **21**, 7447–7454 (2001).

44. Rossi, E.A. & Roorda, A. The relationship between visual resolution and cone spacing in the human fovea. *Nat. Neurosci.* **13**, 156–157 (2010).

ONLINE METHODS

Implant fabrication. Photovoltaic arrays were manufactured on silicon-on-insulator wafers using a six-mask lithographic process, as described previously[13]. To produce anodic-first pulses of electric current, the n-doped and p-doped regions in the diodes were reversed compared to the previous description. Photovoltaic arrays consisted of 70-μm-wide pixels, separated by 5-μm trenches (**Fig. 1a**).

Infrared projection system for *in vitro* recordings. For experiments *in vitro*, the infrared projection system consisted of a polarization-scrambled array of NIR (880 nm) laser diodes coupled into a 400-μm multimode fiber (Dilas M1F4S22-880.3-30C-SS2.1). We collimated the laser beam at the output of the fiber, and used a 2° divergence microlens array diffuser to improve beam homogeneity. Visible light from a yellow (591-nm) LED was coupled into the same optical path using a dichroic mirror. We used an amplitude modulation transmissive LCD screen (Holoeye HEO-0017) to form the images that were projected on the retina through the camera port of an inverted microscope (Olympus IX-71, with a 5× objective). We controlled the image on the LCD display via Matlab using the Psychophysics Toolbox v3. We controlled the timing, width and amplitude of the light pulses using a National Instruments USB-6353 data acquisition card and custom software.

We estimated visible light receptive fields by projecting a flickering binary white noise stimulus with constant mean illumination on the photoreceptor layer of the retina[22]. The spatiotemporal monochromatic white noise stimulus consisted of 100×60 square pixels with each pixel 70 μm on a side, refreshed every 33.33 ms. We randomly set the relative intensity level for each pixel in each frame above or below the 0.5 mean background level at 0.5 ± 0.48. The corresponding contrast, $(I_{max} - I_{min})/(I_{max} + I_{min})$, was therefore 96%, where I_{max} and I_{min} are the maximum and minimum intensities, respectively. The light flux at the gray background level was equivalent to 22000 photons/μm²/s[1] produced by a monochromatic source of wavelength 591 nm.

We estimated electrical receptive fields by projecting a sparse white noise stimulus on the implant, so that the stimulation order of different pixels was randomized but no more than one pixel was activated at any given time. The laser operated with 8-ms pulses at a 2-Hz repetition rate. We chose irradiance levels of 10 mW/mm² so that robust responses were elicited in the RGCs without reaching saturation.

For the alternating gratings measurements, we projected square-wave linear gratings with 100% contrast using pulsed visible (10 ms) and NIR (4 ms) light, with 20-Hz flicker frequency, alternating the contrast at 1 Hz. Peak NIR irradiance in these measurements was 5 mW/mm². We used 6 gratings phases for each stripe width (0°, 60°, 120°, 180°, 240° and 300°). We did not align the gratings with respect to the implant; therefore, relative orientation of the gratings and the implant varied from preparation to preparation, but not within a single preparation. Grating stripe width and phase varied between trials and the order of the gratings presentation in each experiment was randomized.

Electrophysiological recordings *in vitro*. We obtained male and female rats with retinal degeneration from a Royal College of Surgeons (RCS) colony[45] maintained at the Stanford animal facility (P100–P150, $n = 9$, with $n = 3$ for eRF measurements, $n = 4$ for grating measurements and $n = 2$ for frequency characterization). Both male and female RCS rats exhibit the retinal dystrophy phenotype[46], and we used a mix of male and female rats for all experiments. We purchased adult, female Long-Evans WT rats ($n = 8$, with $n = 4$ for eRF measurements, $n = 2$ for gratings measurements and $n = 2$ for frequency characterization) from Charles River Laboratories (Wilmington, MA, USA). All animals were housed with a 12-h light/12-h dark cycle with food and water ad libitum. We conducted all *in vitro* experimental procedures in accordance with the Stanford University Administrative Panel on Laboratory Animal Care and the University of California Santa Cruz Institutional Animal Care and Use Committee guidelines, and conformed to the guidelines of the Association for Research in Vision and Ophthalmology (ARVO) Statement for the Use of Animals in Ophthalmic and Vision research. We killed the animals (390 mg/kg pentobarbital sodium, 50 mg phenytoin sodium) before enucleating one eye. We isolated a small piece of retina (~3 × 3 mm) and placed it between the recording array on the ganglion cell side and the photovoltaic array on the photoreceptor side (**Fig. 1d**,

Supplementary Fig. 1). We perfused the retina with Ames solution (Sigma-Aldrich) saturated in oxygen and kept at 27 °C. We sampled and recorded voltage waveforms at 20 kHz on each of the 512 electrodes of the recording array[17].

***In vitro* data analysis.** We initially subtracted electrical stimulation artifacts from the raw waveform traces (**Supplementary Fig. 2a**), which were subsequently analyzed using custom-written software[17]. We estimated electrical stimulation artifacts by averaging their shape over many (100+) trials. We subsequently aligned the average artifact shape to the raw recordings and pointwise subtracted it from them. This method often led to incomplete artifact removal during the 'light on' phase of the NIR stimulus. Therefore, we blanked this phase in the recordings during data pre-processing. As a consequence, we ignored all possible direct stimulation of RGCs (latency ≤1 ms (ref. 24) in our analysis. Spikes were detected as an event whose amplitude exceeded 4.5 times root-mean-squared (RMS) noise on each electrode. For the purpose of identifying action potentials of individual RGCs, all action potential waveforms underwent dimensionality reduction by principal component analysis before expectation-maximization clustering (**Supplementary Fig. 2b**). We calculated the electrophysiological images (EIs)[17] of the putative neurons by correlating voltage signals recorded over the array with the sorted spike trains (**Supplementary Fig. 2c**). We discarded neurons with abnormal EIs from the analysis: for example, RGCs with multiple axonal tracts. We used the absence of a refractory period in the autocorrelation function to exclude neuron candidates with spike trains contaminated by action potentials from other neurons.

We estimated visual receptive fields by computing the spike-triggered average (STA) response of RGCs to the white noise stimulus projected on the retina. We calculated the STA for each RGC by averaging, over all spikes generated by the neuron, the sequence of stimulus frames preceding each spike[22]. The receptive field (RF) location, size, and orientation were based on the STA frame most significantly different from the mean (gray) background level. We fit this frame with a two-dimensional generalized Gaussian, and we defined the RF diameter as the geometrical mean of the minor and major axes of the 1-s.d. contour of the fitted Gaussian. This representation assumes that the STA is separable in space and time. We estimated the time filters of each neuron, which we used for functional classification by the STA time courses. We calculated these filters by averaging together the time courses of all STA pixels significantly different from the mean intensity level (a significant pixel was defined as one that differs in absolute value from the mean level by more than three times its RMS noise).

For WT retinas, we used the presence of visible RF mosaics underneath the prosthesis to check that the tissue was in healthy physiological condition throughout the recording (**Supplementary Fig. 2d**). We identified functional cell types following techniques previously described in the literature[41]. Briefly, we performed clustering on an array of indicators, including receptive field diameter, shape of the autocorrelation function and time filter of the neurons to group them into functional cell types. Two mosaics found underneath the implant are shown in **Supplementary Figure 2d**.

For electrical stimulation, in order to detect deviations from the spontaneous firing rate that are half its s.d. or larger with a P value of 0.01 and a statistical power of 0.8, a minimum of $n = 94$ trials is required[47]. We constructed peristimulus time histograms (PSTHs) by binning spikes over 5-ms periods and averaged over 100–200 trials (**Supplementary Fig. 2e,f**). We defined the steady-state activity as the 300–500 ms period post stimulus. For eRFs, for each 5-ms time bin in the first 300 ms of the signal, we compared the distribution of the spiking rate to the spontaneous spiking. If the two sets differed statistically ($P < 0.01$, two-sample Kolmogorov-Smirnov test), we considered the response as positive and defined its amplitude as the positive variation from the steady state (in number of spikes). We then constructed the eRF by encoding with gray levels the total number of action potentials elicited in the first 300 ms by each pixel (**Supplementary Fig. 2e**). We fit the eRFs with a two-dimensional Gaussian function and used the 1-s.d. contour to determine the eRF diameter (WT, $n = 92$ neurons across 4 preparations; RCS, $n = 48$ neurons across 3 preparations). The analysis included experimental preparations in which at least 10 RGCs underneath the implant responded to full field stimulation, with at least one action potential elicited per stimulus of 4 ms in duration at 5 mW/mm² irradiance and 2 Hz repetition rate.

Putative correlations between eRF and vRF diameters were hard to evaluate for the following reasons. Variability in the vRF diameters of cells responding to both NIR and visible light stimulation was ±30 μm. Photovoltaic pixels are 70 μm in size; therefore the noise introduced by the uncertainty of the cell position relative to the pixel is expected to dominate measurements of any putative correlation between eRF and vRF diameters. Additionally, we estimated vRF shapes from a 2D Gaussian fit that fails to capture the complex receptive field structure of retinal ganglion cells[48], and the Gaussian approximation introduces further noise in the measurement. Recording from a population of cells with a larger spread in vRF diameters would improve the signal-to-noise ratio of the measurement, thereby presumably allowing us to check for the presence or absence of this correlation. Unfortunately, the efficiency of detecting these RGCs with smaller vRFs is low in our *in vitro* preparations, preventing us from conclusively determining whether a correlation between eRF and vRF diameters exists.

For alternating grating measurements, we obtained the response by integrating the spikes in the 250 ms following the image transition and subtracting the spikes in the 250 ms before the transition. We measured these responses for different phases of the gratings and defined the amplitude of the response to a particular grating width as the maximum response across all phases. We plotted this amplitude as a function of the grating stripe width and fitted a bell-shaped curve (gamma distribution) to the data. For each neuron, we defined the resolution threshold as the smallest grating size that elicited more than 0.5 action potentials per contrast reversal. We performed a kernel density estimate of the threshold distribution with kernel width 4.5 μm and 10 μm for the visible and NIR distributions, respectively (WT, $n = 278$ neurons across 2 preparations; RCS, $n = 109$ neurons across 4 preparations). The investigators were not blinded to allocation during experiments and outcome assessment of the *in vitro* experiments.

In vivo implantation. For *in vivo* experiments, assuming that variability between animals is similar to the measurement noise level, a minimum sample size of 4 is required to detect a VEP signal amplitude 2 s.d. above the noise with a P value of 0.05 and a statistical power of 0.8 (ref. 47). We successfully implanted 16 animals ($n = 9$ male Long-Evans and $n = 7$ female and male RCS), which were all included in this study. We operated on animals at a mean age of 41 days (range 35–58 days). The subretinal implantation technique was similar to the one previously reported by our group[14]. We anaesthetized animals with a mixture of ketamine (75 mg/kg) and xylazine (5 mg/kg) injected intramuscularly. We made a 1.5-mm incision through the sclera and choroid 1.5 mm posterior to the limbus, lifted the retina with an injection of saline solution, and inserted the implant into the subretinal space. We sutured the sclera and conjunctiva with nylon 10-0 and applied topical antibiotic (Bacitracin/Polymyxin B) on the eye post operatively. We conducted all *in vivo* experimental procedures in accordance with the Stanford University institutional guidelines and conformed to the guidelines of the Association for Research in Vision and Ophthalmology (ARVO) Statement for the Use of Animals in Ophthalmic and Vision research.

In vivo imaging. We evaluated the anatomical integration of the device in the subretinal space by OCT (HRA2-Spectralis, Heidelberg Engineering, Heidelberg, Germany) using periodic examinations beginning 1 week after surgery. We performed autofluorescence imaging and fluorescein angiography using the HRA2-Spectralis system (cSLO with 488-nm blue excitation and 500-nm green emission). We conducted fluorescence angiography following intraperitoneal injection of 0.2 mg/kg fluorescein sodium diluted in balanced salt solution.

Implantation of cortical electrodes. We implanted three skull screw electrodes similarly to a previously published technique[49], and secured them in place with cyanoacrylate glue and dental acrylic. We placed two electrodes over the visual cortex, one on each hemisphere, 4 mm lateral from midline, 6 mm caudal to the bregma. We implanted one reference electrode 2 mm right to the midline and 2 mm anterior to the bregma. Nose and tail needle electrodes served as a reference and the ground, respectively. Recordings started 2 weeks after the subretinal implantation.

Anesthesia during recordings. We anaesthetized rats with a mixture of ketamine (37.5 mg/kg) and xylazine (2.5 mg/kg) injected intramuscularly. We took the following steps to assure steady anesthesia: we periodically checked spontaneous eye movements and respiratory pattern, administered supplementary injections of half the initial dose every 45 min or as needed, and limited recording sessions to 120 min per session. We used a heating pad to maintain the body temperature at $37.5 \pm 0.5\,°C$. We conducted electrophysiological recordings with a dim-room illumination of 250 nW/cm^2.

Retinal stimulation *in vivo*. The stimulation system (**Fig. 5c**) included a single-mode pigtailed NIR (915 nm) laser diode and a visible light (532 nm) laser diode coupled into a 1-mm-diameter optical fiber. The collimated output beam illuminated a Digital Micro-mirror Device (DMD, DLP Light Commander, LOGIC PD) to form the patterns. We mounted the optical system on a slit lamp (Zeiss SL–120) to allow direct observation of the patterns on the retina. Following pupil dilation, we covered the cornea with a viscoelastic gel and a cover slip to cancel the optical power of the eye and ensure good retinal visibility. Ocular retraction was required in some cases to help align the implant with the beam. We monitored the position of the light pattern (1 mm in diameter) on the retina with a charge-coupled device (CCD) camera mounted on the same slit lamp. We applied NIR stimulation with pulse durations ranging from 1 to 20 ms and peak irradiances from 0.06 to 4 mW/mm^2. We generated light patterns (linear gratings) with custom software and grating sizes that ranged from 6 to 200 μm per stripe. We alternated these gratings (contrast reversal) at 1 Hz, while pulsing the light sources at 40 Hz using 4-ms flashes at 4 mW/mm^2 and 100 nW/mm^2 for the 915 nm and 532 nm wavelengths, respectively. We performed contrast measurements using a 40-Hz carrier frequency and 1-Hz alternation between irradiance levels I_{max} and I_{min}. We defined the contrast as $(I_{max} - I_{min})/(I_{max} + I_{min})$. We kept the average peak irradiance for these measurements at 2 mW/mm^2. The *in vivo* experiments were not randomized.

VEP recording and analysis. We recorded VEP signals with an Espion E2 system (Diagnosys Inc, Lowell, MA) at a 1 kHz sampling rate using a 0.5- to 500-Hz bandpass filter, and averaged over 250 trials for each experiment. A detectable VEP response was defined as a deviation from the baseline by more than 6 times the noise level. This noise level was determined as the RMS (s.d.) of the signal during the 50 ms preceding the stimulus. We defined cortical thresholds for the full-field stimuli (1 mm in diameter) using 10-ms pulses as the minimum light intensity for which the VEP response was detectable during the first 100 ms after the pulse. We measured modulation of the VEP amplitude by light intensity using 10-ms pulses and normalized to the response at 1 mW/mm^2. We measured modulation of the cortical response by pulse duration using a constant irradiance of 4 mW/mm^2. We recorded from all animals 1–7 months post-implantation. The investigators were not blinded to allocation during experiments and outcome assessment of the *in vivo* experiments.

Visual acuity measurements. We assessed visual acuity by recording the cortical response to alternating gratings of various spatial frequencies, as described previously[26]. In experiments with WT animals stimulated by visible light, grating stripe width varied from 6 to 200 μm ($n = 7$). For accurate assessment of the noise level, we applied a 40-Hz notch filter to remove oscillations due to the flicker, which appear at high grating frequencies. We defined the VEP amplitude as the difference between the maximum and minimum of the cortical signal during the first 300 ms post stimulus. For infrared stimulation, grating sizes varied from 25 to 200 μm per stripe (25, 50, 100, 150, 200 μm, $n = 7$) with an additional measurement at 75 μm/stripe in $n = 3$ animals. The eVEP response was faster than the visible light response, and we measured its amplitude during the first 100 ms post stimulus. For statistical analysis we normalized the VEP amplitude for each grating size to the maximum amplitude in each animal. We defined the noise level as the normalized amplitude at the smallest grating size (6 μm for visible light and 25 μm for NIR). We fitted the plot of the normalized VEP amplitude as a function of the stripe width with a 2nd-degree polynomial function using the 50, 100, 150, 200 μm data points for visible light and the 75, 100, 150, 200 μm data points for prosthetic stimulation. We defined the visual acuity limit as the intersection point of the fitted curve with the noise level. We calculated the uncertainties in the acuity by computing the 3×3 covariance matrix of the polynomial fitting parameters and combining this error with the noise uncertainty,

assuming independence. For the polynomial fit $y(x) = p_1x^2 + p_2x + p_3$ and noise level $y(x) = p_4$, the estimator of the intersection is defined by

$$\hat{x} = \frac{-p_2 \pm \sqrt{p_2^2 - 4p_1(p_3 - p_4)}}{2p_1}$$

Its variance can be calculated as $\sigma^2 = D\Sigma D^T$ with

$$D = \left(\frac{\partial \hat{x}}{\partial p_i}\right) i \in [\![1,4]\!]$$

and Σ the 4×4 covariance matrix of the polynomial fit parameters and the noise level.

For comparison, we also used gaussian, sigmoidal and gamma ($y(x) = axe^{-((x-x_0)/\sigma)^2}$) functions to fit the data and extrapolate visual acuity. Among the functions tested, the second-order polynomial yielded the most conservative estimate of the acuity (**Supplementary Fig. 7**) and it matched previously reported values for electrophysiological and behavioral acuity in normally sighted pigmented rats.

To make sure that responses to the shifting gratings were not due to the change the in the total amount of light between the two phases of the grating, we also measured the cortical responses to full-field illumination with various steps of contrast. Animals with prosthetic stimulation had contrast sensitivity lower than 60% (**Supplementary Fig. 5**), while the total amount of light on the implant did not change by more than 30% during alternation of the largest gratings, and with narrower grating stripes it was much smaller. This confirms that responses to alternating gratings are not due to the difference in total luminance between the two grating phases.

Ocular safety with high power near infrared. Stimulation thresholds ($\sim$1 mW/mm^2) exceed the maximum natural irradiance on the retina ($\sim$1 μW/mm^2) by a factor of 1,000. To avoid any problems with the perception of bright light by the remaining photoreceptors, we used invisible near-infrared (NIR) light within the wavelength range of 880–915 nm. We verified that such NIR illumination did not cause any response of the retina in the absence of an implant (**Supplementary Fig. 6a**).

Ocular safety of the NIR radiation has been described in several prior publications[12,14]. Briefly, NIR light (880–915 nm) is absorbed primarily by pigmented tissues, such as the retinal pigment epithelium, with a practically negligible absorption in transparent ocular tissues. According to ocular safety standards[33], for a single-pulse exposure of duration (t) and NIR wavelength (λ), the peak irradiance limit (P_{peak}) is described by the equation $P_{peak} = 6.93 \times 10^{-4}C_TC_Et^{-0.25}$, where $C_T = 10 \times 0.002^{(\lambda-700)}$ and $C_E = 29.3$ W/mm^2. In our case, with $t = 10$ ms and $\lambda = 905$ nm, the maximum irradiance is 160 mW/mm^2, more than two orders of magnitude above the threshold.

The maximum average irradiance (P_{avg}) that may be delivered chronically to the retina is calculated as $P_{avg} = 6.93 \times 10^{-5}C_TC_E$. For $\lambda = 905$ nm, the average irradiance limit is 5.2 mW/mm^2. Therefore, even the maximum settings used in this *in vivo* study (Peak = 4 mW/mm^2, $t = 4$ ms, and repetition rate of 40 Hz, corresponding to $P_{avg} = 0.64$ mW/mm^2) were still one order of magnitude below the ocular safety limit. In a realistic use case, the average power would be further reduced by the sparseness of the encoded visual scene (for example, by a factor of 2 for the black-and-white square grating used in this study) and by the use of additional levels of gray, below the maximum irradiance in the image.

45. Strauss, O., Stumpff, F., Mergler, S., Wienrich, M. & Wiederholt, M. The Royal College of Surgeons rat: an animal model for inherited retinal degeneration with a still unknown genetic defect. *Acta Anat.* **162**, 101–111 (1998).
46. LaVail, M.M., Sidman, R.L. & Gerhardt, C.O. Congenic strains of RCS rats with inherited retinal distrophy. *J. Hered.* **66**, 242–244 (1975).
47. Whitley, E. & Ball, J. Statistics review 4: sample size calculations. *Crit. Care* **6**, 335–341 (2002).
48. Field, G.D. *et al.* Functional connectivity in the retina at the resolution of photoreceptors. *Nature* **467**, 673–677 (2010).
49. You, Y., Klistorner, A., Thie, J. & Graham, S. Latency delay of visual evoked potential is a real measurement of demyelination in a rat model of optic neuritis. *Invest. Ophthalmol. Vis. Sci.* **52**, 6911–6918 (2011).